

Quantum defects in 2D transition metal dichalcogenides for THz-technologies

Jingda Zhang^{1,2} and Su Ying Quek^{1,2,3,4,5*}

¹Department of Physics, National University of Singapore, Singapore 117551

²Centre for Advanced 2D Materials, National University of Singapore, Singapore 117546

³Department of Materials Science and Engineering, National University of Singapore, Singapore 117575

⁴Integrative Sciences and Engineering Programme, NUS Graduate School, National University of Singapore, Singapore 119077

⁵NUS College, National University of Singapore, Singapore 138593

*Corresponding author: S.Y.Q. (email: phyqsy@nus.edu.sg)

Abstract

Terahertz technologies are important for a number of emerging applications, such as for next generation communications. We predict that transition metal substitutional defects in two-dimensional transition metal dichalcogenides (TMDs) can serve as quantum defects for terahertz technologies. Central to this prediction is the finding that the zero field splittings between spin sublevels in such defects are typically in the sub-terahertz to terahertz range due to the large spin-orbit coupling in these systems. As a proof of concept, we consider different transition metal impurities from across the periodic table, in prototypical TMDs, MoS₂ and WSe₂. Using first principles calculations, we demonstrate that selected spin triplet defects can potentially serve as qubits operating in the terahertz regime. We also propose defects that can potentially be quantum sources of terahertz radiation. Our research broadens the scope of advancements in quantum information science and lays a foundation for their integration with THz technologies.

Point defects introduce atomic-like electronic states in the band gap of host materials. Defects with states that behave as two-level quantum systems are highly sought after in quantum information science. Such defects are potential quantum emitters, emitting single photons, which are of fundamental significance in quantum information technologies such as quantum key distribution, quantum metrology and quantum computing¹. These defects also provide the framework for the establishment of a qubit, the building block for quantum information²⁻⁴ that replaces the classical bit. Practical implementations of qubits require the ability to initialize and manipulate the state of these defects (e.g., spin states) and the ability to perform measurements with high fidelity^{3,5}. Well-established in solid-state quantum technologies is the nitrogen-vacancy centre (NV⁻ centre) in diamond, which has a spin-triplet ground state. If one of the spin sublevels can be preferentially populated, the quantum states of the electron spins can be coherently manipulated by inducing Rabi oscillations between the spin triplet sublevels⁶ that are split by the zero-field splitting (ZFS) energy. For commonly studied spin defects such as the NV⁻ centre in diamond, the ZFS is dominated by spin-spin dipole-dipole interactions and is typically in the GHz range^{7,8}.

There has been a growing interest in THz technologies, for applications in imaging, sensing, metrology and 6G wireless communications⁹. In particular, although previously, the “terahertz gap” was a region of the spectrum that was more difficult to access, rapid advancements in recent years have led to the development of stable THz sources that have spurred the investigation of many applications¹⁰. Quantum sources of THz radiation are, however, rare, and exploring possible single photon emitters of THz radiation is a topic of current interest¹¹. Such quantum THz emitters would pave the way for the development of THz quantum photonic technologies, and bring THz communications and metrology to the next level by introducing additional controls in the quantum regime. On the other hand, qubits operating in the THz instead of GHz regime have the advantage of a larger energy separation between the spin sublevels, which translates into longer spin relaxation times, potentially increasing the coherence and stability of the spin states, enabling more robust quantum memory technologies¹²⁻¹⁴. Resonant optical excitation techniques, used for low temperature high fidelity initialization and read-out of qubits¹⁵, may also be potentially employed at higher temperatures in the THz regime compared to the GHz regime.

Two-dimensional (2D) solid-state materials offer significant advantages for single photon emitters and high-performance optically-addressable defect systems due to their ease of

integration with optoelectronic and nanophotonic components¹⁶⁻¹⁸. Quantum emitters in 2D materials also benefit from a low level of total internal reflection, leading to higher light extraction efficiencies, and the possibility of enhancing the emission strength by integration with cavities^{19,20} and photonic waveguides or plasmonic structures¹. Among the 2D materials, 2D transition metal dichalcogenides (TMDs) in particular are promising host platforms¹⁸ because of their semiconducting nature which allows for gate-tunability²¹, and the existence of scalable and highly controlled strategies for uniformly incorporating point defects involving substitutional transition metal (TM) atoms in 2D TMDs²²⁻²⁴.

Here, we show that substitutional TM point defects in 2D TMDs have remarkably large ZFS, typically in the sub-THz to THz range. We identify defects that are candidates for spin qubits operating in the THz range. We further identify defects in which optical pumping followed by intersystem crossing results in population inversion within the spin multiplet for the triplet ground state, opening up possibilities for these point defects to function as single photon THz emitters. The defect candidates discussed here were uncovered using a first principles materials discovery approach in which 25 different TM atoms were incorporated into MoS₂ and WSe₂. This work bridges the field of quantum information science with THz technologies.

Results and Discussion

Transition metal (TM) substitutional defects in monolayer TMDs

The pristine monolayer (ML) 2H-TMDs, MoS₂ and WSe₂, exhibit D_{3h} point group symmetry with each Mo or W atom having a trigonal prismatic coordination with adjacent chalcogen atoms. To create substitutional point defects, we replace one Mo or W atom in a 4×4×1 supercell with a 3d, 4d or 5d TM element from group IVB to IIB across the periodic table (excluding the radioactive technetium) (Fig. 1a). The key results have also been checked with a larger 6×6×1 supercell (see Supplementary Note 1). The introduction of the TM substitutional defect can sometimes disrupt the original trigonal prismatic coordination due to changes in the positions of the TM dopant and adjacent chalcogen atoms. Such Jahn-Teller distortion has also been reported in the literature^{25,26}. In this work, the point groups of the relaxed defect systems are predominantly D_{3h} (no distortion), C_{2v} and C_{1h}, the symmetry operations of which are

shown in Fig. 1b-c. The identification of the point groups aids in the analysis of the optical selection rules and of the in-gap electronic wavefunctions.

Defect charge transition levels

Defects in semiconductors can exhibit different stable charge states, depending on the value of the Fermi level relative to the thermodynamic charge transition levels (CTLs). Assessing different charge states allows us to look for defects with spin triplet ground states – the simplest spin configuration that exhibits ZFS. We compute the CTLs of the 25 TM dopants in ML MoS₂ (Fig. 2a) and WSe₂ (Fig. 2b) using DFT with the PBE exchange-correlation functional²⁷, and refine the results for selected quantum defect candidates using the more accurate HSE06 functional²⁸.

Starting from the first group to the right of Mo and W (vertical lines in Fig. 2), the (0/-1) and (+1/0) CTLs generally shift down as the group corresponding to the TM dopant shifts right across the periodic table to Group IIB, and this trend continues as we loop back to Group IVB, followed by Group VB (Fig. 2). These trends make sense because dopants with fewer valence electrons than elements in group VIB (Cr/Mo/W) have a tendency to accept electrons in MoS₂ and WSe₂, while those with more valence electrons tend to lose electrons. Nevertheless, it is evident that, for a considerable number of elements, the neutral, -1 and +1 charge states can all be stabilized with an appropriate Fermi level in the band gap.

Spin-triplet ground states

To identify defects with spin triplet ground states, we compute the energy differences ΔE between the singlet and triplet states of the defect systems with an even number of electrons. We use the PBE functional to compute ΔE (Supplementary Tables 3 and 4) and identify 19 defect systems that are predicted to have a spin triplet ground state using PBE (Supplementary Table 5). Of these, one system (Co⁺¹-MoS₂) exhibits the C₁ symmetry where there are no symmetry-forbidden transitions and is not interesting as a candidate qubit or quantum emitter. To facilitate the identification of many-body states and group symmetries in order to interpret the radiative and non-radiative transitions, we focus on systems in which the defect states in the band gap are quite clearly separated from one another and from the bulk states in the PBE calculations. For this reason, we focus on 12 of the remaining 18 systems and compute the

singlet-triplet energy differences using HSE06 in these systems (Supplementary Table 6). These calculations reveal that Zn^0 and Hg^0 in ML $\text{MoS}_2/\text{WSe}_2$ possess a slightly more stable singlet state under C_{2v} symmetry than the D_{3h} triplet state (see Supplementary Table 6); the other 8 systems are found to have a triplet ground state. Based on these considerations, we evaluate these 8 defect systems as candidates for quantum defects: Mn^{-1} , Fe^0 , and Cd^0 in both MoS_2 and WSe_2 , as well as Rh^{-1} in MoS_2 and Ir^{-1} in WSe_2 . Henceforth, we shall use the HSE06 functional for all calculations.

Table 1 shows the point group symmetries and singlet-triplet energy differences of the 8 defect candidates obtained using HSE06. Neutral Cd substitutions do not cause substantial distortion of the trigonal prismatic coordination due to their filled orbitals in their electronic configurations, thus retaining the D_{3h} symmetry. However, the other defect states, with partially filled d-orbitals, can interact more strongly with the host lattice and Jahn-Teller distortions result in a reduction in symmetry (Fig. 1b-c), leading to the C_{2v} or C_{1h} point groups.

Zero-field splitting in terahertz range

We now quantify the splitting between spin sublevels in the $S = 1$ states of these 8 defect systems. In the absence of external magnetic fields, the ZFS causes the threefold degeneracy of the $S = 1$ state to be lifted. The spin sublevel eigenstates in the presence of ZFS are the $m_s = 0$ state, labelled by $|0\rangle$, as well as linear combinations, $|+\rangle$ and $|-\rangle$, of the $m_s = \pm 1$ states. $|+\rangle$, $|-\rangle$, and $|0\rangle$ take the form of $\frac{1}{\sqrt{2}}(|\uparrow\uparrow\rangle - |\downarrow\downarrow\rangle)$, $\frac{1}{\sqrt{2}}(|\uparrow\uparrow\rangle + |\downarrow\downarrow\rangle)$, and $\frac{1}{\sqrt{2}}(|\uparrow\downarrow\rangle + |\downarrow\uparrow\rangle)$, respectively, where $|\uparrow\rangle$ and $|\downarrow\rangle$ are along the spin quantization axis. Their corresponding eigenenergies are $\frac{1}{3}D - E$, $\frac{1}{3}D + E$, and $-\frac{2}{3}D$, respectively, where D , the axial component, represents the energy difference between the $|0\rangle$ sublevel and the average energy of the $|+\rangle$ and $|-\rangle$ sublevels, while the rhombic component E describes the energy difference between the $|+\rangle$ and $|-\rangle$ sublevels²⁹ (see also Methods).

The ZFS arises from a spin-spin contribution and a spin-orbit contribution. Similar to other systems such as defects in diamond and SiC^7 , we obtain spin-spin contributions in the GHz range. The large spin-orbit coupling (SOC) in these systems results in a large spin-orbit contribution to the ZFS which we find to be typically in the sub-terahertz to terahertz range (Fig. 3b and Supplementary Table 7). The ZFS values are particularly large for the TM

substitutional defects in WSe₂, due to the larger SOC effect in WSe₂ compared to MoS₂. These ZFS values are significantly larger than those reported in the literature – the NV⁻ centre in diamond and spin defects in silicon carbide and hexagonal boron nitride have ZFS values of less than 10 GHz^{30–32}, while the Ti dopant substituting the divacancy site of ML h-BN has a ZFS value of 19.4 GHz³³, and the defect, Mos, in ML WS₂ has a ZFS value of 21.7 GHz³⁴. The ZFS attributed to SOC is inherently related to the magnetic anisotropy energy of the defect. The value of D^{SO} and E^{SO} can be directly calculated by DFT using the expressions below (see Methods for a derivation):

$$D^{SO} = 2E_{tot}^{DFT}(zz) - [E_{tot}^{DFT}(xx) + E_{tot}^{DFT}(yy)],$$

$$E^{SO} = E_{tot}^{DFT}(xx) - E_{tot}^{DFT}(yy).$$

x , y , and z are defined here to be mutually orthogonal electron spin directions assigned in the DFT calculations, according to the convention that $E_{tot}^{DFT}(zz)$ has the largest difference from $E_{tot}^{DFT}(xx)$ and $E_{tot}^{DFT}(yy)$. The z direction is then the spin quantization axis that originates from SOC interactions in the system. As illustrated in Fig. 3a, if the magnetization prefers to align along the spin quantization axis (i.e., $D^{SO} < 0$, $m_s = \pm 1$ is more stable), it can be referred to as easy-axis magnetization; in contrast, easy-plane anisotropy describes the case when the magnetization aligns within a plane perpendicular to the spin quantization axis ($D^{SO} > 0$).

Spin qubit and THz emitter

The ZFS (~meV/THz) of the spin defects reported here can reduce thermal fluctuations compared to spin defects with ZFS in the GHz range; this reduction in thermal fluctuations is beneficial for maintaining spin coherence of a qubit. As THz sources are now increasingly available⁹, THz radiation can be used to initialize and manipulate the spin through Rabi oscillations between the spin sublevels, if the spin sublevels can be selectively occupied. In order to selectively occupy the spin sublevels in the ground state triplet, two different approaches are typically used. The first is to make use of intersystem crossing (ISC) governed by symmetry selection rules. A classic example is the NV⁻ centre in diamond where non-radiative decay through ISC is stronger for one of the spin channels³⁵. Room temperature spin readout can be achieved by the strength of the photoluminescence signal, due to enhanced non-radiative decay for one of the spin sublevels³⁶. The second is to lower the temperature so that only the lowest energy spin sublevel is occupied. The temperature should also be low enough to distinguish the resonant excitations in different spin channels, and resonant spin-selective

optical excitation is used for spin readout¹⁵. Resonant optical excitation techniques for qubits have the advantage of higher fidelities¹⁵, and are best suited for qubits that have larger ZFS, and where at least one of the spin sublevels does not couple strongly to the singlet state.

We work out the symmetry-allowed and symmetry-forbidden ISC between the triplet and singlet manifolds. ISC between spin sublevels is allowed if $\Gamma_i \otimes \Gamma_{SOC} \otimes \Gamma_f \supset \Gamma_1$, where Γ_i and Γ_f are, respectively, the irreducible representations (IRs) of the initial state and the final state, and Γ_1 is the full symmetric IR³⁷. This implies that ISC is forbidden between spin sublevels with different IR. Optically-allowed radiative transitions within the same manifold couple spin sublevels with the same m_s value. Many-body states are constructed by considering the transfer of a ‘hole’ from lowest energy unoccupied defect levels to the highest energy occupied defect levels^{38,39} or equivalently, the transfer of an electron in the opposite direction (see Supplementary Notes 2-3).

From group theory, we see that ISC does not provide a non-radiative decay path for either spin channel in the triplet for the D_{3h} point group, and similarly, one of the spin channels is not coupled by ISC to the singlet state for the C_{2v} point group (Supplementary Note 2(iii)). Thus, the corresponding defects, Cd, Mn and Fe substitutional defects, are promising as spin qubits operated by resonant optical excitation techniques with high fidelities.

For the C_{1h} point group, ISC selectively couples spin sublevels with different m_s values. Using Ir^{-1} -WSe₂ for illustration, the single-particle defect levels and corresponding excitations are shown in Fig. 4a and the IRs of the many-body singlet and triplet spin sublevels are shown in Fig. 4b. ISC couples all spin sublevels of the first excited $S = 1$ state to the first excited $S = 0$ state, but only the higher energy A'' spin-sublevel in the $S = 1$ ground state is coupled to the $S = 0$ ground state (blue arrows, Fig. 4b). Consequently, the higher-energy A'' spin sublevel can be preferentially populated over the lower energy A' spin sublevel through an optical excitation of the triplet state, followed by non-radiative ISC decay from the $S = 1$ to the $S = 0$ excited state, radiative decay in the singlet manifold, and then ISC decay from the $S = 0$ to the $S = 1$ ground state. This allows for spin initialization of the defect through this optical pumping cycle, and the spin can be controlled using radiation with a ~ 6.5 THz frequency.

If the ISC rates coupling different spin sublevels to the singlet manifold are substantially different, spin readout in $\text{Ir}^{-1}\text{-WSe}_2$ can be achieved through spin-dependent photoluminescence, similar to the room temperature operation of the NV^{-} centre in diamond³⁵. Furthermore, because the higher energy spin sublevel is preferentially populated through the optical excitation cycle, population inversion can be achieved, offering potential for the defect to be a single photon THz emitter driven by near-infrared photons (~ 0.7 eV; see Supplementary Note 3). To achieve this, one can consider using a THz photonic cavity⁴⁰ – emission from single defects has been significantly enhanced using photonic cavities, such as microwave emission using ZFS-split levels in silicon carbide defects^{31,41}, and single photon emission from defects in WSe_2 ^{19,20}.

Similar to $\text{Ir}^{-1}\text{-WSe}_2$, $\text{Rh}^{-1}\text{-MoS}_2$ belongs to the C_{1h} point group and is also a potential candidate as a spin qubit, although details differ. The optical excitation cycle is presented in Supplementary Fig. 2 with accompanying discussion in the caption. In the case of $\text{Rh}^{-1}\text{-MoS}_2$, the ZPL excitation of the triplet state falls within the telecom wavelength range.

We have further investigated the tunability of the ZFS parameter, D^{SO} , as a function of biaxial in-plane strain in $\text{Ir}^{-1}\text{-WSe}_2$ and $\text{Rh}^{-1}\text{-MoS}_2$ (Supplementary Fig. 3). We find that D^{SO} is highly tunable for both $\text{Ir}^{-1}\text{-WSe}_2$ and $\text{Rh}^{-1}\text{-MoS}_2$; D^{SO} in $\text{Ir}^{-1}\text{-WSe}_2$ increases to 10.2 THz at 2% in-plane strain, and D^{SO} in $\text{Rh}^{-1}\text{-MoS}_2$ increases to ~ 0.8 THz at 2% in-plane strain. We also find that the dependence of D^{SO} on in-plane strain is approximately linear, and the predicted strain-dependent ZFS values offer advantages of considerable flexibility with precise control of tunable THz emitters.

We conclude with a few comments on the feasibility of realizing the proposed substitutional defects for spin qubits and THz emitters. In recent years, there have been rapid advancements in the development of scalable approaches to controllably incorporate substitutional point defects in 2D TMDs²²⁻²⁴. MoS_2 is typically found to be an n-type semiconductor, while WSe_2 exhibits ambipolar properties. The advantage of using semiconducting 2D TMDs (compared to materials with larger band gaps) is the relative ease with which the Fermi level can be controlled, for example, using metal contacts⁴², gate control⁴³, chemical doping⁴⁴, and proton irradiation⁴⁵. Fig. 2 shows that the neutral charge state for Cd and Fe substitutional defects, of interest for spin qubits, can be accessed for a range of Fermi levels in the band gap. The

formation energy diagram with the HSE06 functional, including SOC, further confirms that the -1 charge states for $\text{Ir}_W\text{-WSe}_2$ and $\text{Rh}_{\text{M}_0}\text{-MoS}_2$ are accessible (Supplementary Fig. 4). The formation energies of the neutral $\text{Ir}_W\text{-WSe}_2$ and $\text{Rh}_{\text{M}_0}\text{-MoS}_2$ defects are ~ 3.1 eV and ~ 2.5 eV, respectively. Compared to the formation energy of ~ 6 eV for the neutral NV centre in diamond^{4,36}, the smaller but positive values indicate the relative ease at which these defects can be created, while also ensuring that there will not be a massive spontaneous formation of the defects during growth.

Lastly, we acknowledge that further investigations are desirable in areas outside the scope of our current research, particularly in the evaluation of the coherence time for spin qubits, ISC coupling rates, and the strength of the magnetic dipole transitions. However, our theoretical predictions pave the way for these future studies. Furthermore, our findings that large SOC can result in ZFS in the THz range for these defects point toward the potential for finding other defect systems featuring heavy elements that also have a ZFS in the THz range. We anticipate that our work presents avenues for inspiring advancements in a new field of quantum THz technologies.

Methods

DFT computational details. Our spin-polarized DFT calculations are performed using VASP⁴⁶ within the projector-augmented wave⁴⁷ formalism and a plane-wave energy cutoff of 450 eV. For the preliminary screening calculations for appropriate charge states and spin-triplet ground states, we adopt the generalized gradient approximation to the exchange-correlation functional, as parameterized by Perdew, Burke and Ernzerhof (PBE)²⁷. The hybrid Heyd-Scuseria-Ernzerhof (HSE06)^{28,48} functional is used for defect structure relaxations, calculations of zero-field splitting (ZFS), excited-state dynamics and formation energy diagrams of selected candidates. For the defect structure relaxations in the screening process, three initial dopant positions are considered: one at the original centered position, another with a slight in-plane displacement, and a third with a displacement along a tilted out-of-plane direction. We use a $4\times 4\times 1$ supercell, with the Brillouin zone sampled by a $3\times 3\times 1$ Monkhorst-Pack k-mesh. We have also checked our results with a $6\times 6\times 1$ supercell using a $2\times 2\times 1$ k-mesh (see Supplementary Note 1). A 15-Å-thick vacuum layer is included to avoid image interaction in the z-direction. The structures are relaxed until the magnitudes of the forces are less than

0.005 eV/Å for PBE and 0.02 eV/Å for HSE06, respectively. The VASPKit code⁴⁹ is used in the data analysis for plotting band structures and visualization of wavefunctions.

Defect formation and charge transition levels. The defect formation energy is computed following⁵⁰:

$$E^f [TM_{\text{Mo/W}}^q] = E_{\text{tot}} [TM_{\text{Mo/W}}^q] - E_{\text{tot}} [\text{Pristine}] + \mu_{\text{Mo/W}} - \mu_{\text{TM}} + q(\varepsilon_F + E_{\text{VBM}}) + \Delta_q.$$

TM stands for transition metal impurities. E_{tot} is the total energy of the defect and pristine system. μ is the chemical potential for the element species. Comments on the chemical potentials used are provided in the discussion accompanying Supplementary Fig. 4. ε_F is the Fermi level referenced to E_{VBM} , the VBM of the pristine cell. Δ_q represents the charge-dependent finite-size correction by Freysoldt-Neugebauer-Van de Walle (FNV)⁵¹ calculated using the `sxdefectalign2d` tool⁵² to eliminate the artificial electrostatic interaction between the periodic defect images and background charge. The CTLs can therefore be computed as:

$$\varepsilon_F(q + 1/q) = (E_{\text{tot}}[TM^{q+1}] + \Delta_{q+1}) - (E_{\text{tot}}[TM^q] + \Delta_q) - E_{\text{VBM}}.$$

Zero-field splitting. The first order ZFS contributed by spin-spin dipole interactions is calculated by adding the hidden tag “LDMATRIX” implemented in VASP⁸.

The second-order SOC-contributed ZFS has the spin Hamiltonian of²⁹

$$\hat{H}_{\text{ZFS}} = D^{\text{SO}} \left(\hat{S}_z^2 - \frac{1}{3} S(S+1) \right) + E^{\text{SO}} (\hat{S}_x^2 - \hat{S}_y^2) = \hat{D}^{\text{SO}} + \hat{E}^{\text{SO}},$$

which yields, for $S = 1$, $\frac{1}{3}D^{\text{SO}} + E^{\text{SO}}$, $\frac{1}{3}D^{\text{SO}} - E^{\text{SO}}$, and $-\frac{2}{3}D^{\text{SO}}$ for $|+\rangle$, $|-\rangle$ and $|0\rangle$ eigenstates, respectively (see main text).

For a single spin, with the spin-quantization axis in the z-direction, and spin states $|z\rangle \equiv |\uparrow\rangle$ and $| -z\rangle \equiv |\downarrow\rangle$, we have

$$|x\rangle = \frac{1}{\sqrt{2}}(|\uparrow\rangle + |\downarrow\rangle),$$

$$|y\rangle = \frac{1}{\sqrt{2}}(|\uparrow\rangle + i|\downarrow\rangle).$$

Thus, for two spins in the $S = 1$ system,

$$|xx\rangle = |x\rangle \otimes |x\rangle = \frac{1}{2}(|\uparrow\uparrow\rangle + |\downarrow\downarrow\rangle) + \frac{1}{2}(|\uparrow\downarrow\rangle + |\downarrow\uparrow\rangle),$$

$$|yy\rangle = |y\rangle \otimes |y\rangle = \frac{1}{2}(|\uparrow\uparrow\rangle - |\downarrow\downarrow\rangle) + \frac{1}{2}i(|\uparrow\downarrow\rangle + |\downarrow\uparrow\rangle).$$

Therefore, using the Hamiltonian $\hat{H}_{\text{ZFS}} + \hat{H}_{\text{elec}}$, the total energies are:

$$E_{\text{tot},xx}^{\text{DFT}} = -\frac{1}{6}D^{\text{SO}} + \frac{1}{2}E^{\text{SO}} + E_{\text{el}},$$

$$E_{tot,yy}^{DFT} = -\frac{1}{6}D^{SO} - \frac{1}{2}E^{SO} + E_{el},$$

$$E_{tot,zz}^{DFT} = \frac{1}{3}D^{SO} + E_{el},$$

where E_{el} is introduced as the total electronic energy, which we assume to be independent of the orientation of the spins. Now, the value of D^{SO} and E^{SO} can be directly calculated by DFT through:

$$D^{SO} = 2E_{tot,zz}^{DFT} - [E_{tot,xx}^{DFT} + E_{tot,yy}^{DFT}],$$

$$E^{SO} = E_{tot,xx}^{DFT} - E_{tot,yy}^{DFT}.$$

For the calculation of total energies, we first carry out a self-consistent collinear calculation without SOC. Reading from the ground-state charge density of the system, the SOC can be treated as a perturbation in non-self-consistent calculations. The total energy of the system is self-consistently calculated including SOC with a convergence threshold of 10^{-9} eV for different spin orientations⁵³.

Excited-state calculations. The optical transition energies are computed by the constrained DFT method⁵⁴. The vertical absorption, vertical emission and ZPL energies are used to construct the schematic configuration coordinate diagram⁵⁵ in Supplementary Fig. 9.

Data availability

The data that support the findings of this study are available within the paper and Supplementary Information. Additional relevant data are available from the corresponding authors upon reasonable request.

References

1. Aharonovich, I., Englund, D. & Toth, M. Solid-state single-photon emitters. *Nat Photonics* **10**, 631–641 (2016).
2. Dreyer, C. E., Alkauskas, A., Lyons, J. L., Janotti, A. & Van de Walle, C. G. First-principles calculations of point defects for quantum technologies. *Annu Rev Mater Res* **48**, 1–26 (2018).
3. Wolfowicz, G. *et al.* Quantum guidelines for solid-state spin defects. *Nat Rev Mater* **6**, 906–925 (2021).
4. Weber, J. R. *et al.* Quantum computing with defects. *Proceedings of the National Academy of Sciences* **107**, 8513–8518 (2010).
5. Awschalom, D. D., Hanson, R., Wrachtrup, J. & Zhou, B. B. Quantum technologies with optically interfaced solid-state spins. *Nat Photonics* **12**, 516–527 (2018).
6. Hanson, R., Gywat, O. & Awschalom, D. D. Room-temperature manipulation and decoherence of a single spin in diamond. *Phys Rev B* **74**, 161203 (2006).
7. Biktagirov, T., Schmidt, W. G. & Gerstmann, U. Calculation of spin-spin zero-field splitting within periodic boundary conditions: Towards all-electron accuracy. *Phys Rev B* **97**, 115135 (2018).
8. Ivády, V., Simon, T., Maze, J. R., Abrikosov, I. A. & Gali, A. Pressure and temperature dependence of the zero-field splitting in the ground state of NV centers in diamond: A first-principles study. *Phys Rev B* **90**, 235205 (2014).
9. Dhillon, S. S. *et al.* The 2017 terahertz science and technology roadmap. *J Phys D Appl Phys* **50**, 043001 (2017).
10. Markelz, A. G. & Mittleman, D. M. Perspective on terahertz applications in bioscience and biotechnology. *ACS Photonics* **9**, 1117–1126 (2022).
11. Groiseau, C., Domínguez, A. I. F., Cano, D. M. & Muñoz, C. S. Single-photon source over the terahertz regime. *arXiv preprint arXiv:2305.11754* (2023).
12. Ye, S. & Neese, F. How do heavier halide ligands affect the signs and magnitudes of the zero-field splittings in halogenonickel(II) Scorpionate Complexes? A Theoretical Investigation Coupled to Ligand-Field Analysis. *J Chem Theory Comput* **8**, 2344–2351 (2012).
13. Schulte, K. A., Vignesh, K. R. & Dunbar, K. R. Effects of coordination sphere on unusually large zero field splitting and slow magnetic relaxation in trigonally symmetric molecules. *Chem Sci* **9**, 9018–9026 (2018).
14. Zabala-Lekuona, A., Seco, J. M. & Colacio, E. Single-Molecule Magnets: From Mn₁₂-ac to dysprosium metallocenes, a travel in time. *Coord Chem Rev* **441**, 213984 (2021).
15. Robledo, L. *et al.* High-fidelity projective read-out of a solid-state spin quantum register. *Nature* **477**, 574–578 (2011).
16. Ping, Y. & Smart, T. J. Computational design of quantum defects in two-dimensional materials. *Nat Comput Sci* **1**, 646–654 (2021).

17. Bertoldo, F., Ali, S., Manti, S. & Thygesen, K. S. Quantum point defects in 2D materials-the QPOD database. *NPJ Comput Mater* **8**, 56 (2022).
18. Zhang, G., Cheng, Y., Chou, J.-P. & Gali, A. Material platforms for defect qubits and single-photon emitters. *Appl Phys Rev* **7**, 031308 (2020).
19. Iff, O. *et al.* Purcell-enhanced single photon source based on a deterministically placed WSe₂ monolayer quantum dot in a circular Bragg grating cavity. *Nano Lett* **21**, 4715–4720 (2021).
20. Drawer, J.-C. *et al.* Monolayer-Based Single-Photon Source in a Liquid-Helium-Free Open Cavity Featuring 65% Brightness and Quantum Coherence. *Nano Lett* (2023) doi:10.1021/acs.nanolett.3c02584.
21. Jing, Y. *et al.* Tunable electronic structure of two-dimensional transition metal chalcogenides for optoelectronic applications. *Nanophotonics* **9**, 1675–1694 (2020).
22. Shen, D. *et al.* Synthesis of Group VIII Magnetic Transition-Metal-Doped Monolayer MoSe₂. *ACS Nano* **16**, 10623–10631 (2022).
23. Loh, L., Zhang, Z., Bosman, M. & Eda, G. Substitutional doping in 2D transition metal dichalcogenides. *Nano Res* **14**, 1668–1681 (2021).
24. Kozhakhmetov, A. *et al.* Scalable Substitutional Re-Doping and its Impact on the Optical and Electronic Properties of Tungsten Diselenide. *Advanced Materials* **32**, 2005159 (2020).
25. Fang, M. & Yang, E.-H. 2D Magnetic Semiconductors via Substitutional Doping of Transition Metal Dichalcogenides. *arXiv preprint arXiv:2303.11173* (2023).
26. Ramasubramaniam, A. & Naveh, D. Mn-doped monolayer MoS₂: An atomically thin dilute magnetic semiconductor. *Phys Rev B* **87**, 195201 (2013).
27. Perdew, J. P., Burke, K. & Ernzerhof, M. Generalized gradient approximation made simple. *Phys Rev Lett* **77**, 3865 (1996).
28. Heyd, J., Scuseria, G. E. & Ernzerhof, M. Hybrid functionals based on a screened Coulomb potential. *J Chem Phys* **118**, 8207–8215 (2003).
29. Mostafanejad, M. Basics of the spin Hamiltonian formalism. *Int J Quantum Chem* **114**, 1495–1512 (2014).
30. Christle, D. J. *et al.* Isolated spin qubits in SiC with a high-fidelity infrared spin-to-photon interface. *Phys Rev X* **7**, 021046 (2017).
31. Fischer, M. *et al.* Highly efficient optical pumping of spin defects in silicon carbide for stimulated microwave emission. *Phys Rev Appl* **9**, 054006 (2018).
32. Gottscholl, A. *et al.* Spin defects in hBN as promising temperature, pressure and magnetic field quantum sensors. *Nat Commun* **12**, 4480 (2021).
33. Smart, T. J., Li, K., Xu, J. & Ping, Y. Intersystem crossing and exciton–defect coupling of spin defects in hexagonal boron nitride. *NPJ Comput Mater* **7**, 59 (2021).
34. Lee, Y. *et al.* Spin-defect qubits in two-dimensional transition metal dichalcogenides operating at telecom wavelengths. *Nat Commun* **13**, 7501 (2022).

35. Gruber, A. *et al.* Scanning confocal optical microscopy and magnetic resonance on single defect centers. *Science (1979)* **276**, 2012–2014 (1997).
36. Gali, Á. Ab initio theory of the nitrogen-vacancy center in diamond. *Nanophotonics* **8**, 1907–1943 (2019).
37. Penfold, T. J., Gindensperger, E., Daniel, C. & Marian, C. M. Spin-vibronic mechanism for intersystem crossing. *Chem Rev* **118**, 6975–7025 (2018).
38. Abdi, M., Chou, J.-P., Gali, A. & Plenio, M. B. Color centers in hexagonal boron nitride monolayers: a group theory and ab initio analysis. *ACS Photonics* **5**, 1967–1976 (2018).
39. Maze, J. R. *et al.* Properties of nitrogen-vacancy centers in diamond: the group theoretic approach. *New J Phys* **13**, 025025 (2011).
40. Messelot, S. *et al.* Tamm cavity in the terahertz spectral range. *ACS Photonics* **7**, 2906–2914 (2020).
41. Kraus, H. *et al.* Room-temperature quantum microwave emitters based on spin defects in silicon carbide. *Nat Phys* **10**, 157–162 (2014).
42. Liu, W. *et al.* Role of metal contacts in designing high-performance monolayer n-type WSe₂ field effect transistors. *Nano Lett* **13**, 1983–1990 (2013).
43. Allain, A. & Kis, A. Electron and hole mobilities in single-layer WSe₂. *ACS Nano* **8**, 7180–7185 (2014).
44. Ji, H. G. *et al.* Chemically tuned p- and n-type WSe₂ monolayers with high carrier mobility for advanced electronics. *Advanced Materials* **31**, 1903613 (2019).
45. Liang, H. *et al.* Robust n-type doping of WSe₂ enabled by controllable proton irradiation. *Nano Res* **16**, 1220–1227 (2023).
46. Kresse, G. & Furthmüller, J. Efficient iterative schemes for ab initio total-energy calculations using a plane-wave basis set. *Phys Rev B* **54**, 11169 (1996).
47. Blöchl, P. E. Projector augmented-wave method. *Phys Rev B* **50**, 17953 (1994).
48. Krukau, A. V., Vydrov, O. A., Izmaylov, A. F. & Scuseria, G. E. Influence of the exchange screening parameter on the performance of screened hybrid functionals. *J Chem Phys* **125**, 224106 (2006).
49. Wang, V., Xu, N., Liu, J.-C., Tang, G. & Geng, W.-T. VASPKIT: A user-friendly interface facilitating high-throughput computing and analysis using VASP code. *Comput Phys Commun* **267**, 108033 (2021).
50. Freysoldt, C. *et al.* First-principles calculations for point defects in solids. *Rev Mod Phys* **86**, 253 (2014).
51. Freysoldt, C., Neugebauer, J. & Van de Walle, C. G. Fully ab initio finite-size corrections for charged-defect supercell calculations. *Phys Rev Lett* **102**, 016402 (2009).
52. Freysoldt, C. & Neugebauer, J. First-principles calculations for charged defects at surfaces, interfaces, and two-dimensional materials in the presence of electric fields. *Phys Rev B* **97**, 205425 (2018).

53. Biktagirov, T. & Gerstmann, U. Spin-orbit driven electrical manipulation of the zero-field splitting in high-spin centers in solids. *Phys Rev Res* **2**, 023071 (2020).
54. Kaduk, B., Kowalczyk, T. & Van Voorhis, T. Constrained density functional theory. *Chem Rev* **112**, 321–370 (2012).
55. Alkauskas, A., Yan, Q. & Van de Walle, C. G. First-principles theory of nonradiative carrier capture via multiphonon emission. *Phys Rev B* **90**, 075202 (2014).

Acknowledgement

The project is supported from the Ministry of Education (MOE), Singapore, under grant number MOE2018-T3-1-005. The authors acknowledge computational resources at the CA2DM cluster and at the National Supercomputing Centre (NSCC) in Singapore. We also thank Y. Chen, N.L.Q. Cheng, K. Ulman and G. Eda for discussions.

Author contributions

J.Z. performed the calculations and data analysis under the supervision of S.Y.Q. All authors contributed to the discussion and writing of this paper.

Competing interests

The authors declare no competing interests.

Additional information **Supplementary information**

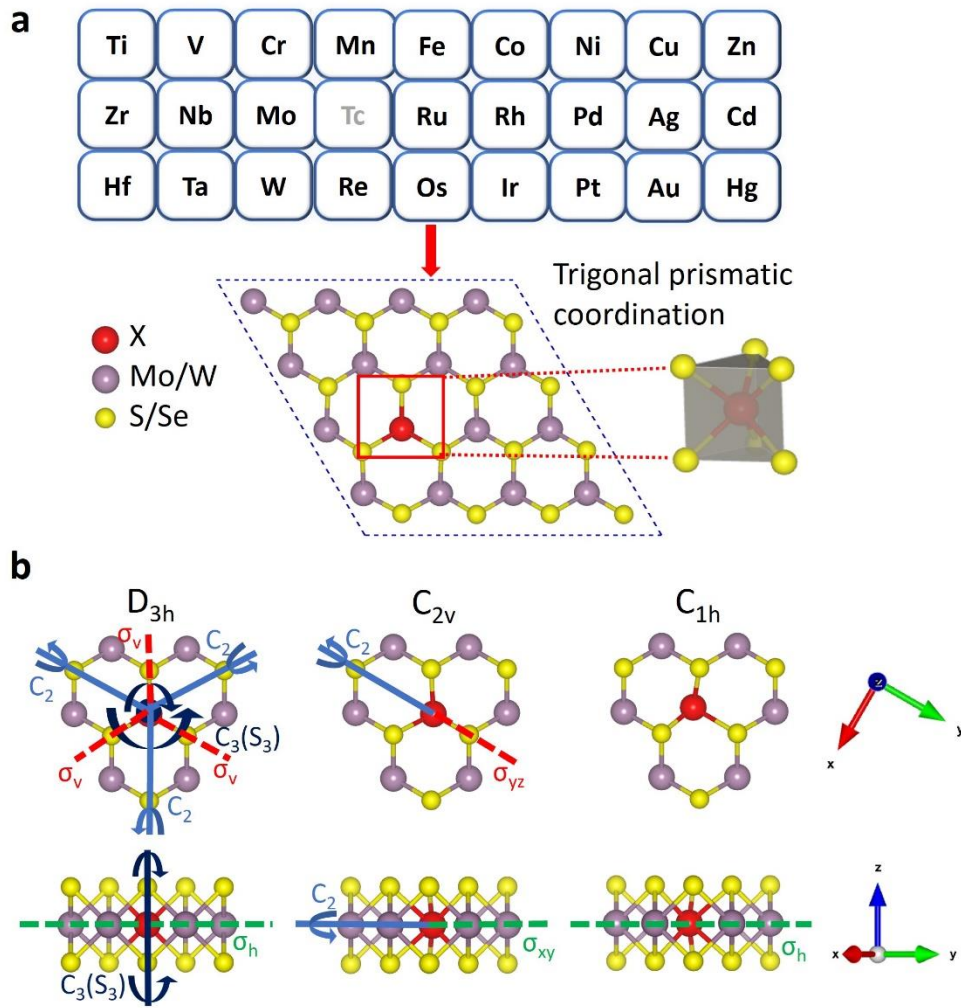


Fig. 1 a Schematic showing the creation of a substitutional defect where one Mo/W atom in a 4×4 supercell of monolayer 2H-MoS₂/2H-WSe₂ is replaced by TM atom X. The trigonal prismatic coordination shown here represents the initial atomic structure before structural relaxation. **b** Top views (top) and side views (bottom) of the possible local atomic structure and symmetries for the TM substitutional defects after structural relaxation.

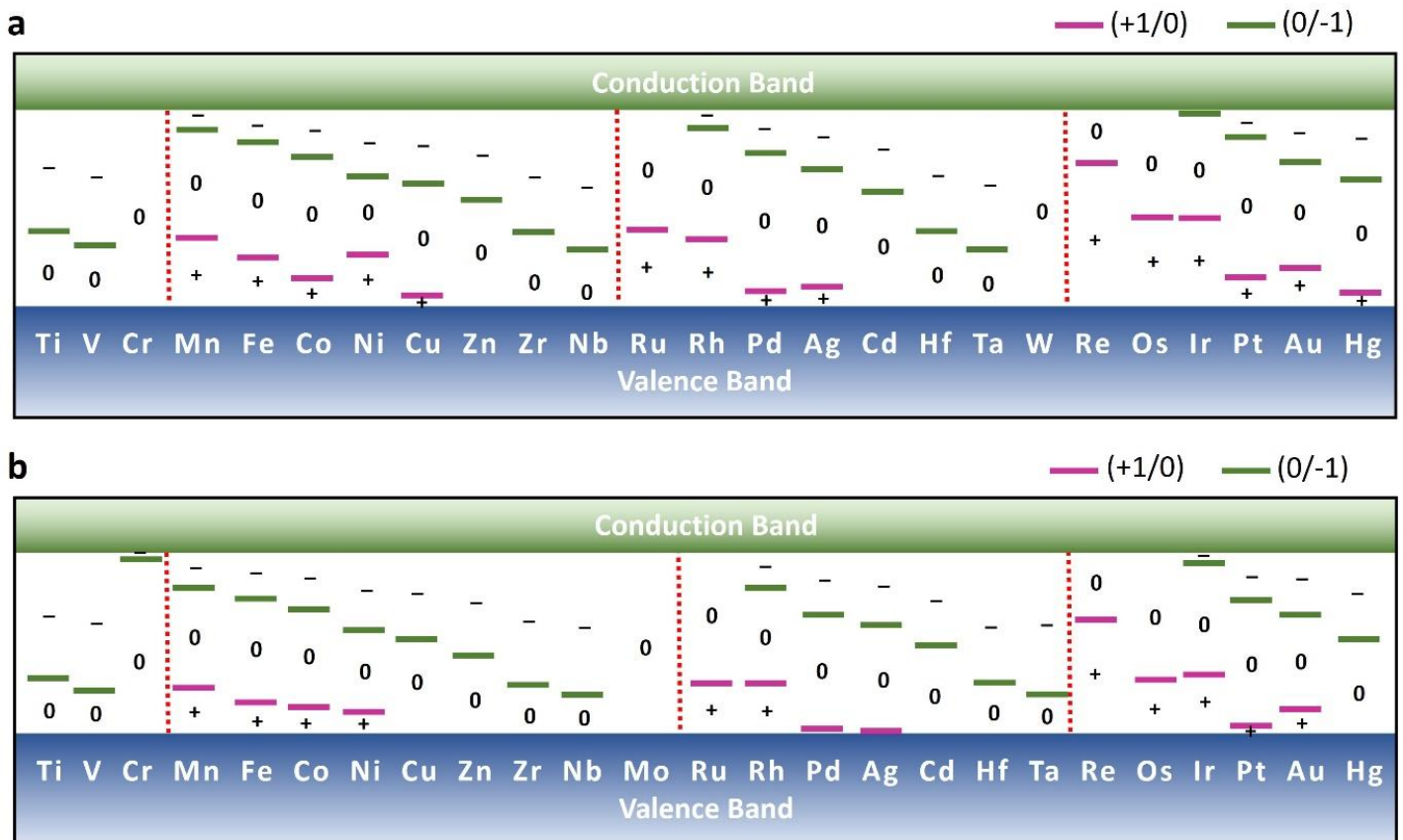


Fig. 2 Thermodynamic charge transition levels (CTLs) for TM substitutional defects in ML **a** MoS₂ and **b** WSe₂. The vertical axis is energy, and the CTL energies are aligned with the valence band maximum (VBM; PBE band gaps are used here) of the pristine TMD. (+1/0) levels (purple) and (0/-1) levels (green) denote the transition levels from the charge state +1 to 0, and from 0 to -1, respectively. 0, +, and - indicate the neutral, +1, and -1 charge state within the Fermi level range. Based on calculations on a few defects (see also Supplementary Fig. 4), the higher charge states are unlikely to be stable for Fermi levels within the band gap in these systems. The Group VIB elements (eg. Mo, W, Cr) are marked with a vertical dotted line on their right. See Supplementary Tables 1 and 2 for the CTL values.

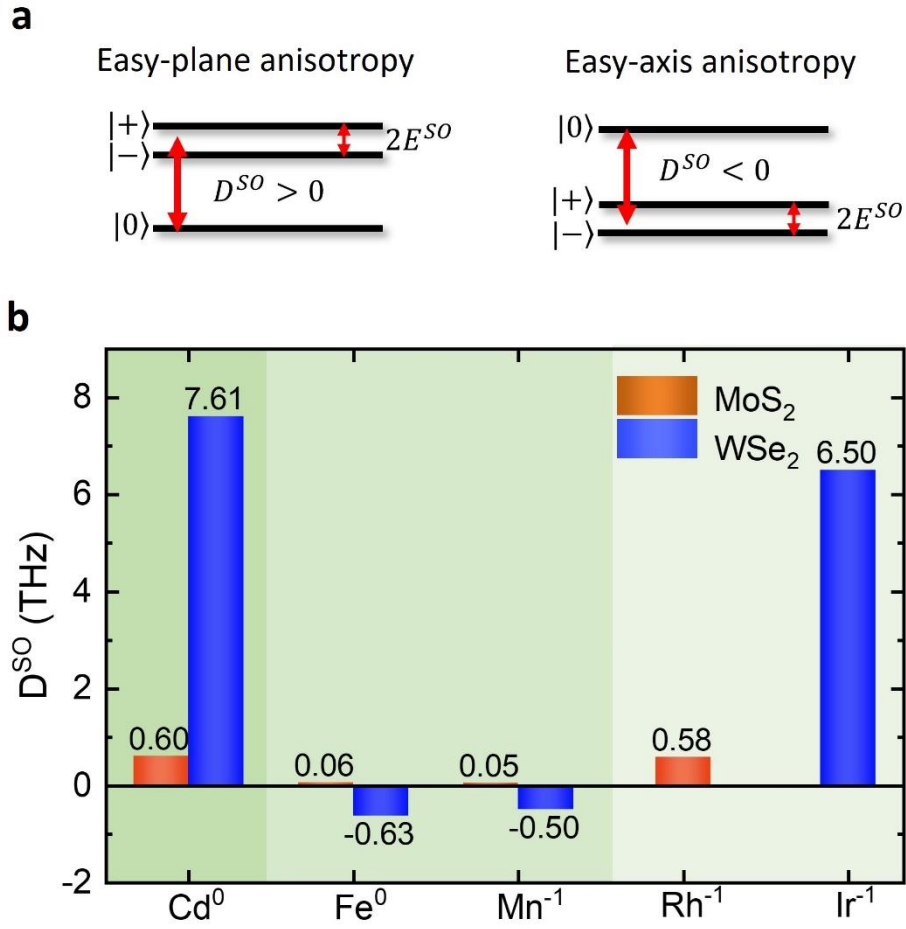


Fig. 3 a Spin sublevel diagram for spin-triplet state for easy-plane and easy-axis magnetic anisotropy. **b** D^{SO} values of ZFS for TM dopants in ML MoS₂ and WSe₂. The background shading of dark, medium, and light green represents the D_{3h} , C_{2v} and C_{1h} symmetries of the defects.

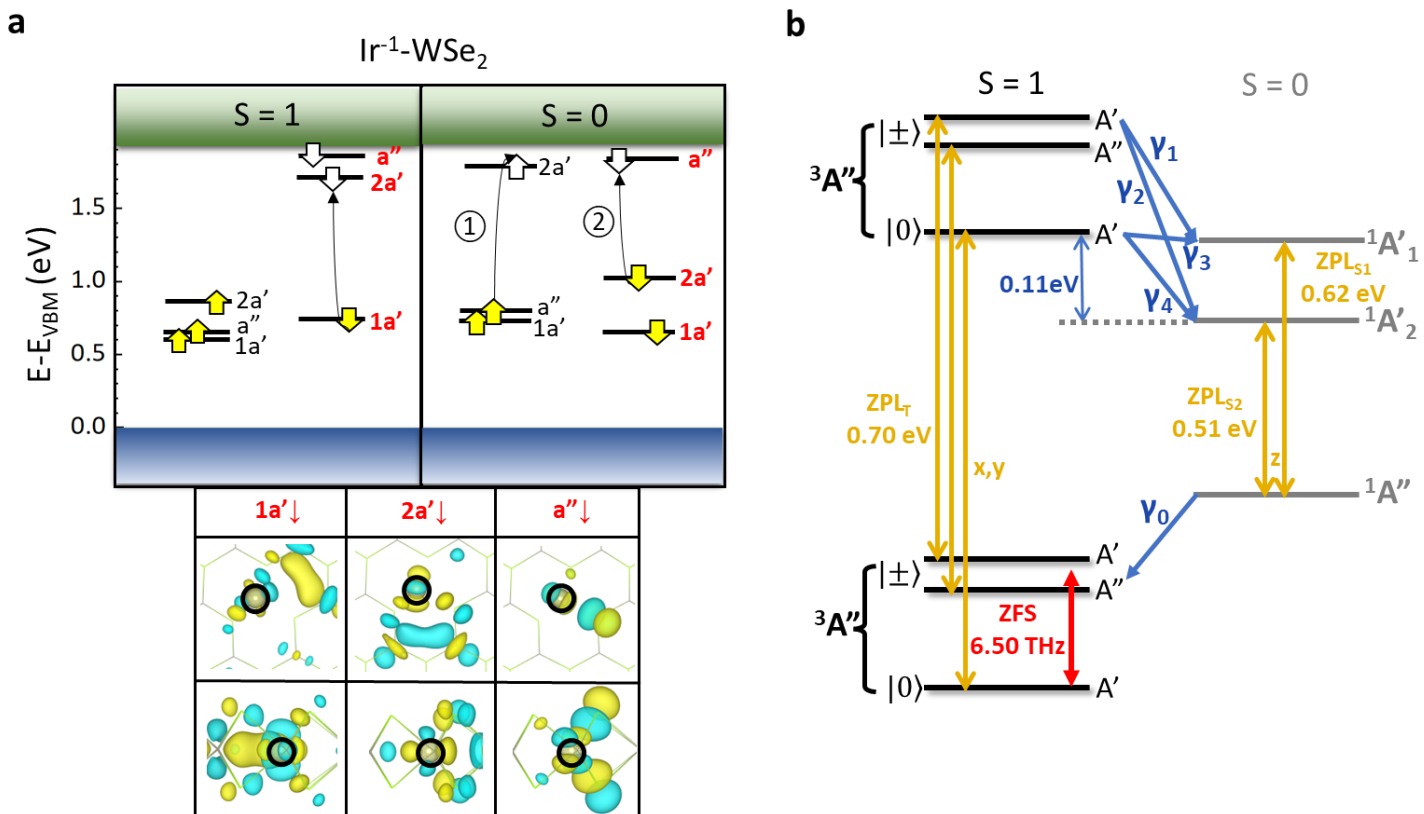


Fig. 4 **a** Single-particle Kohn-Sham defect states and wavefunctions of Ir⁻¹-WSe₂. The yellow solid and hollow arrows mark the occupied and unoccupied in-gap defect states, respectively, which are labelled according to their IRs transforming under group symmetry. The black arrows denote the excitations leading to the many-body states in **b**. The directions of the arrows correspond to electron transfer. Two excitation processes marked by ① and ② are considered for the singlet. The corresponding real part of wavefunctions at the Gamma point are visualized in the top-view (top) and side-view (bottom) with an isosurface value of 30% of the maximum. The defect sites are circled in black. **b** Many-body level structure of Ir⁻¹-WSe₂, with intersystem crossing pathways γ_0 , γ_1 , γ_2 , γ_3 , and γ_4 (blue), the ZFS splitting (red), and the ZPL for optically-allowed transitions with polarized photons (yellow), indicated. The subscript T, S1 and S2 denote the ZPL transitions for spin triplet and singlet configurations, respectively.

TM defect	Charged state	Symmetry	ΔE (Singlet-Triplet) (eV)
Host - MoS₂			
Mn	-1	C _{2v}	0.76
Rh	-1	C _{1h}	0.12
Fe	0	C _{2v}	0.22
Cd	0	D _{3h}	0.34
Host - WSe₂			
Mn	-1	C _{2v}	0.68
Ir	-1	C _{1h}	0.08
Fe	0	C _{2v}	0.17
Cd	0	D _{3h}	0.32

Table 1 Singlet-triplet energy differences ΔE of TM substitutional defects in ML TMDs calculated by the HSE06 functional. Positive values indicate that the $S = 1$ (triplet state) is more stable. Point group symmetries are identified by the local geometry around the defect and visualization of defect states. For the defects shown in this table, both the singlet and triplet configurations have the same point group symmetries.

Supplementary Table 1 Thermodynamic charge transition levels (CTLs) for TM defects in ML MoS₂ (PBE)

MoS ₂	CTL (+1/0) (eV)	CTL (0/-1) (eV)	Stable charge states with even number of electrons
Ti	-0.38	0.67	0
V	-0.39	0.56	-1
Cr	-0.43	1.88	0
Mn	0.58	1.55	-1, +1
Fe	0.39	1.42	0
Co	0.24	1.30	-1, +1
Ni	0.42	1.12	0
Cu	0.08	1.08	-1, +1
Zn	-0.08	0.95	0
Zr	-0.39	0.65	0
Nb	-0.39	0.50	-1
Ru	0.63	1.87	0
Rh	0.57	1.56	-1, +1
Pd	0.13	1.34	0
Ag	0.16	1.19	-1, +1
Cd	-0.03	1.01	0
Hf	-0.38	0.66	0
Ta	-0.37	0.52	-1
W	-0.44	2.26	0
Re	1.22	2.07	+1
Os	0.74	2.02	0
Ir	0.74	1.68	+1
Pt	0.22	1.47	0
Au	0.31	1.30	-1, +1
Hg	0.11	1.11	0

Supplementary Table 2 Thermodynamic charge transition levels for TM defects in ML WSe₂ (PBE)

WSe ₂	CTL (+1/0) (eV)	CTL (0/-1) (eV)	Stable charge states with even number of electrons
Ti	-0.44	0.44	0
V	-0.51	0.36	-1
Cr	-0.53	1.51	0
Mn	0.39	1.24	-1, +1
Fe	0.26	1.16	0
Co	0.21	1.07	-1, +1
Ni	0.17	0.90	0
Cu	-0.03	0.82	+1
Zn	-0.16	0.68	0
Zr	-0.45	0.39	0
Nb	-0.56	0.32	-1
Mo	-0.53	1.95	0
Ru	0.42	1.55	0
Rh	0.43	1.25	-1, +1
Pd	0.04	1.03	0
Ag	0.05	0.94	-1, +1
Cd	-0.12	0.77	0
Hf	-0.44	0.41	0
Ta	-0.55	0.34	-1
Re	0.97	1.60	-1, +1
Os	0.48	1.68	0
Ir	0.55	1.49	-1, +1
Pt	0.05	1.15	0
Au	0.20	1.03	-1, +1
Hg	-0.02	0.83	0

Supplementary Table 3 Singlet-triplet energy differences ΔE for TM defects in ML MoS₂ (PBE)

MoS ₂	Charged state	ΔE (Singlet-Triplet) (eV)
V	-1	-1.62
Mn	-1	0.26
Mn	+1	-0.91
Co	-1	0.08
Co	+1	0.07
Cu	-1	0.06
Cu	+1	-0.07
Nb	-1	-1.78
Rh	-1	0.08
Rh	+1	-0.12
Ag	-1	-0.07
Ag	+1	-0.10
Ta	-1	-1.76
Re	+1	-1.68
Ir	-1	-0.10
Ir	+1	-0.20
Au	-1	-0.02
Au	+1	-0.11
Ti	0	-0.11
Cr	0	-1.15
Fe	0	0.13
Ni	0	-0.45
Zn	0	0.07
Zr	0	-0.12
Ru	0	-0.20
Pd	0	-0.13
Cd	0	0.08
Hf	0	-0.12
W	0	-1.82
Os	0	-0.25
Pt	0	-0.14
Hg	0	0.09

Supplementary Table 4 Singlet-triplet energy differences ΔE for TM defects in ML WSe₂ (PBE)

WSe ₂	Charged state	ΔE (Singlet-Triplet) (eV)
V	-1	-1.51
Mn	-1	0.30
Mn	+1	-0.73
Co	-1	0.10
Co	+1	0.03
Cu	-1	0.06
Cu	+1	0.04
Nb	-1	-1.70
Rh	-1	-0.26
Rh	+1	-0.16
Ag	-1	-0.12
Ag	+1	0.04
Ta	-1	-1.62
Re	-1	-0.29
Re	+1	-1.44
Ir	-1	0.06
Ir	+1	-0.21
Au	-1	0.00
Au	+1	-0.08
Ti	0	0.01
Cr	0	-0.92
Fe	0	0.32
Ni	0	-0.07
Zn	0	0.08
Zr	0	-0.02
Mo	0	-1.77
Ru	0	-0.24
Pd	0	-0.10
Cd	0	0.08
Hf	0	-0.03
Os	0	-0.33
Pt	0	-0.11
Hg	0	0.08

Supplementary Table 5 Singlet-triplet energy differences ΔE of selected spin-triplet candidates (PBE)

TM Defect	Charged state	Symmetry	ΔE (Singlet-Triplet) (eV)
Host - MoS₂			
Co	+1	C₁	0.07
Mn	-1	C _{2v}	0.26
Co	-1	C _{1h}	0.08
Cu	-1	C _{2v}	0.06
Rh	-1	C _{1h}	0.08
Fe	0	C _{2v}	0.13
Zn	0	D _{3h}	0.07
Cd	0	D _{3h}	0.08
Hg	0	D _{3h}	0.09
Host - WSe₂			
Cu	+1	C _{2v}	0.04
Ag	+1	C _s	0.04
Mn	-1	C _{2v}	0.30
Co	-1	C _{1h}	0.10
Cu	-1	C _{1h}	0.06
Ir	-1	C _{1h}	0.06
Fe	0	C _{2v}	0.32
Zn	0	D _{3h}	0.08
Cd	0	D _{3h}	0.08
Hg	0	D _{3h}	0.08

Note that the Co⁺¹-MoS₂ shows C₁ symmetry with only identity element, which does not have symmetry-forbidden transitions.

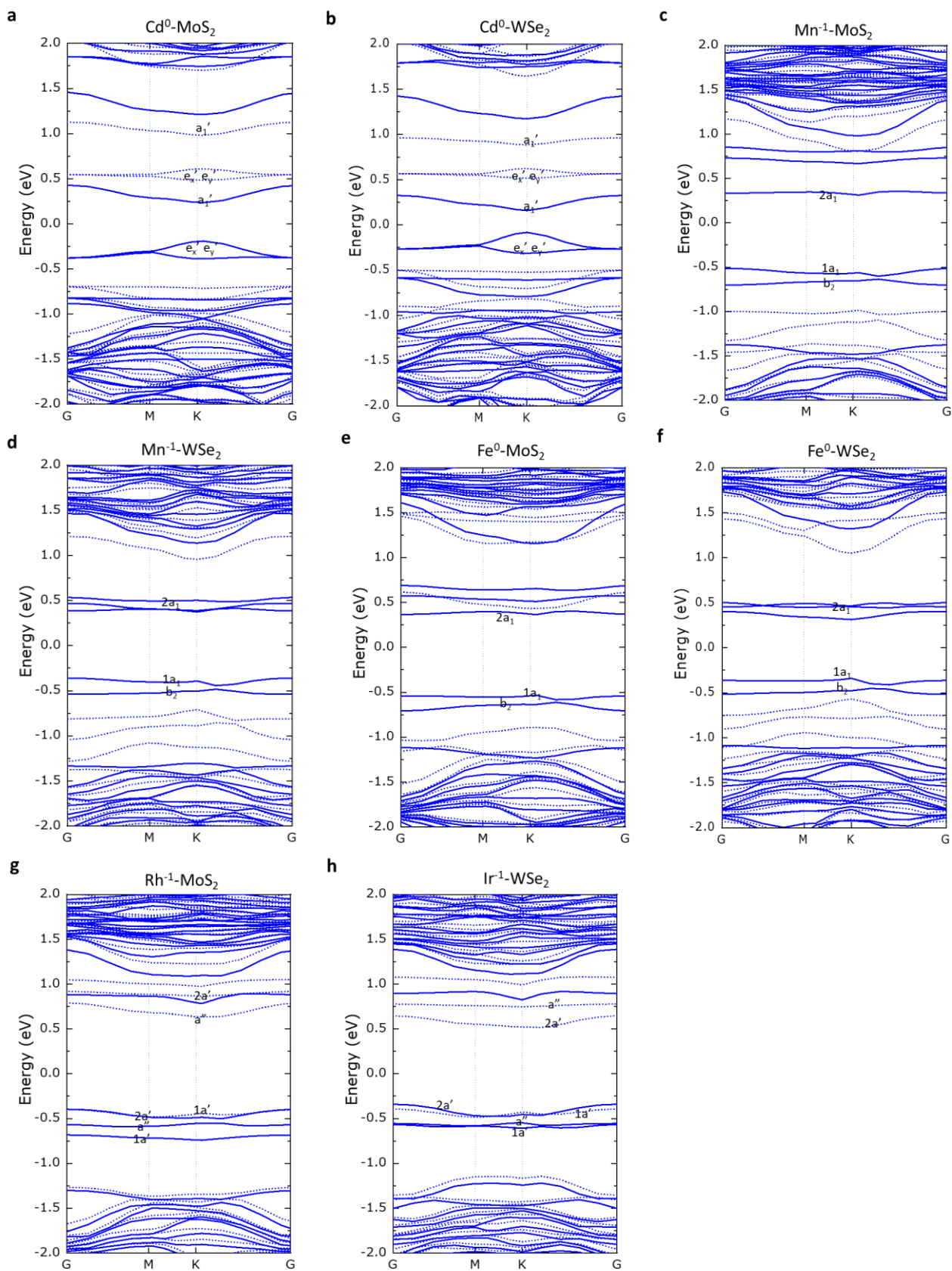
Supplementary Table 6 Selected TM defects in ML TMDs (HSE06)

TM Defect	Charged state	Symmetry	ΔE (Singlet-Triplet) (eV)
Host - MoS₂			
Mn	-1	C _{2v}	0.76
Rh	-1	C _{1h}	0.12
Fe	0	C _{2v}	0.22
Zn	0	D _{3h}	0.37 (-0.04)
Cd	0	D _{3h}	0.34 (0.00)
Hg	0	D _{3h}	0.34 (-0.03)
Host - WSe₂			
Mn	-1	C _{2v}	0.68
Ir	-1	C _{1h}	0.08
Fe	0	C _{2v}	0.44
Zn	0	D _{3h}	0.34 (-0.06)
Cd	0	D _{3h}	0.32 (0.02)
Hg	0	D _{3h}	0.32 (-0.05)

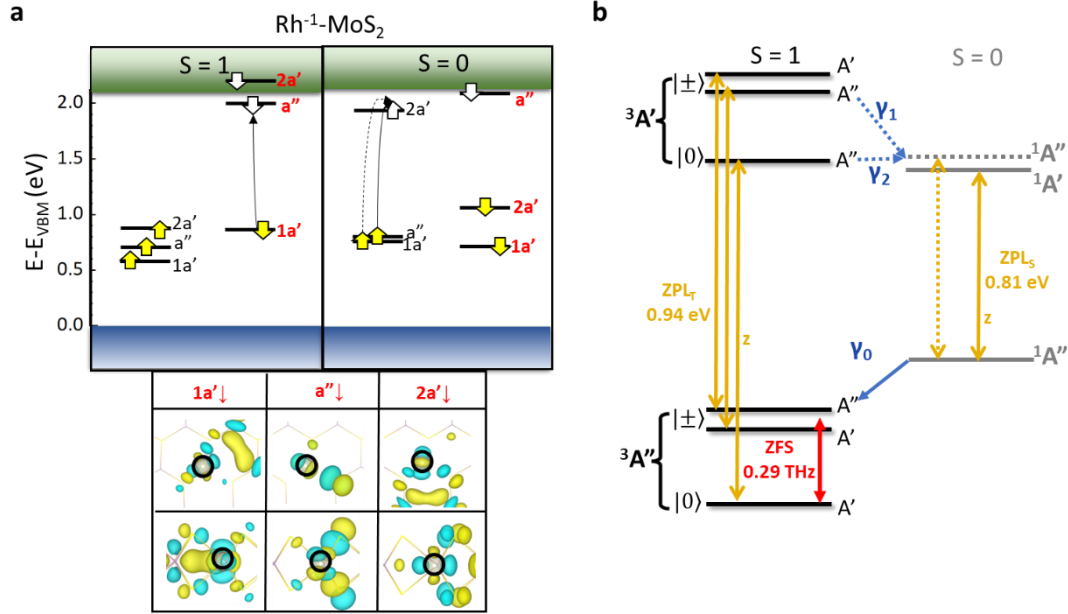
Note that the entries in red do not have spin triplet ground states. The numbers in brackets are negative and indicate the energy differences between a singlet state in a different point group symmetry, and the triplet state. It was found that the singlet states with C_{2v} symmetry were more stable in these four cases.

Supplementary Table 7 Zero-field splitting (ZFS) values for TM defects in ML MoS₂ and WSe₂ (HSE06)

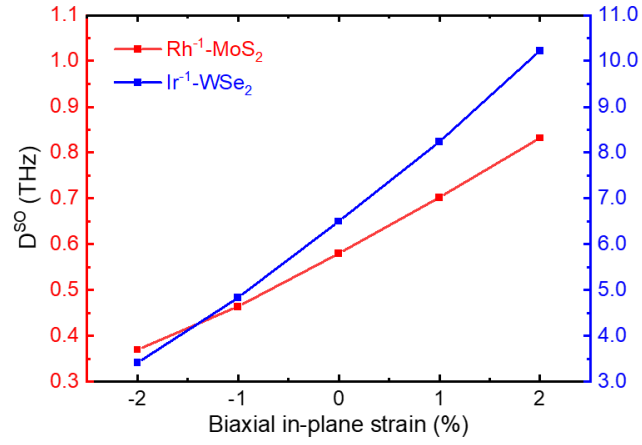
TM defects	Charged state	Symmetry	D ^{SO} (GHz)	D ^{SS} (GHz)	E ^{SO} (GHz)	E ^{SS} (GHz)	D ^{tot} (THz)
Host - MoS₂							
Cd	0	D _{3h}	601.00	1.30	0.08	0.00	0.60
Fe	0	C _{2v}	55.06	14.12	2.84	0.55	0.07
Mn	-1	C _{2v}	45.50	19.71	-19.42	0.20	0.07
Rh	-1	C _{1h}	579.24	0.87	-57.06	0.26	0.58
Host - WSe₂							
Cd	0	D _{3h}	7609.02	1.14	2.33	0.06	7.61
Fe	0	C _{2v}	-625.94	33.89	-33.75	4.11	-0.59
Mn	-1	C _{2v}	-496.24	26.66	-23.13	1.51	-0.47
Ir	-1	C _{1h}	6501.48	-0.59	33.45	-0.07	6.50



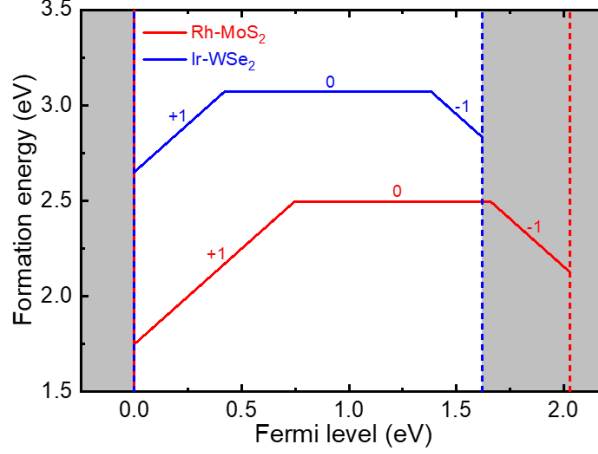
Supplementary Fig. 1 Band structures for selected defect candidates (HSE06). The solid and dashed lines indicate the spin up and spin down states, respectively. The irreducible representations (IRs) of crucial defect states are denoted.



Supplementary Fig. 2 Electronic structure for Rh⁻¹-MoS₂. (a) Single-particle Kohn-Sham defect states and wavefunctions of Rh⁻¹-MoS₂. The yellow solid and hollow arrows mark the occupied and unoccupied in-gap defect states, respectively, which are labelled according to their IRs transforming under group symmetry. The black arrows denote the excitations leading to the many-body states in b. The directions of the arrows correspond to electron transfer. The corresponding real part of wavefunctions at the Gamma point are visualized in the top-view (top) and side-view (bottom) with an isosurface value of 30% of the maximum. The defect sites are circled in black. (b) Many-body level structure of Rh⁻¹-MoS₂, with the ISC pathways γ_0 , γ_1 , and γ_2 (blue), the ZFS splitting (red), and the ZPL transitions with polarized photons (yellow), indicated. The subscript T and S denote the ZPL transitions for spin triplet and singlet configurations, respectively. Note that for Rh⁻¹-MoS₂, unlike Ir⁻¹-WSe₂, we do not consider excitation to the spin down a'' state in the $S = 0$ case due to its proximity to the conduction band. Instead, the second excitation of the spin-up, corresponding to the $|^1A''\rangle$ is relevant and can help achieve the selective spin initialization and population inversion. However, since the first excited state of $|^1A'\rangle$ is almost as high as the triplet excited state, this prediction is subject to verification with more extensive calculations.



Supplementary Fig. 3 ZFS value as a function of in-plane strain. D^{SO} of $\text{Rh}^1\text{-MoS}_2$ and $\text{Ir}^1\text{-WSe}_2$ vs biaxial in-plane strain from -2% to 2%.



Supplementary Fig. 4 Formation energy diagram of Rh_{Mo} in MoS_2 and Ir_{W} in WSe_2 obtained using HSE06 calculations. The dashed lines indicate the VBM and CBM of ML MoS_2 (red) and ML WSe_2 (blue). The VBM of both systems are aligned. Only charge states with the lowest formation energies are shown. The higher charge states (+2, -2, etc.) are found to be unstable for Fermi levels within the band gap.

Note that the formation energies are determined with chemical potential μ under constraint conditions:

$$\begin{aligned}\mu_M + 2\mu_X &= E[\text{MX}_2] \\ \mu_{\text{TM}} + 2\mu_X &\leq E[(\text{TM})\text{X}_2] \\ \mu_M &\leq E[\text{M}] \\ \mu_X &\leq E[\text{X}] \\ \mu_{\text{TM}} &\leq E[\text{TM}]\end{aligned}$$

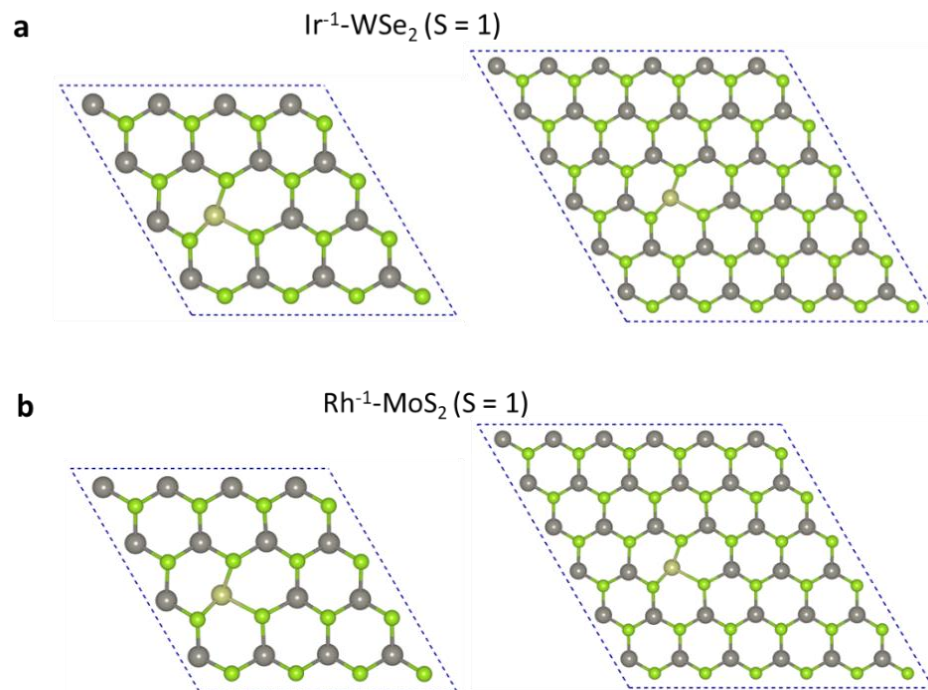
Here, $M = \text{Mo/W}$, $X = \text{S/Se}$, $\text{TM} = \text{Rh/Ir}$. The boundary for the least limit of formation energy can be derived as:

$$(\mu_M - \mu_{\text{TM}})_{\min} = E[\text{MX}_2] - E[(\text{TM})\text{X}_2].$$

To avoid the uncertainty of μ_{TM} values from experiments, we also demonstrate by PBE calculation that the formation energy of Ir_{W} (Rh_{Mo}) is lowered by 6.79 (6.03) eV compared to the sum of formation energy of vacancy, Vac_{W} (Vac_{Mo}) and adsorption, Ir_{ad} (Rh_{ad}). This indicates that with the introduction of TM impurities, the formation of substitutional defects is energetically more favorable.

Supplementary Note 1: A comparative study of supercell sizes (4×4 vs 6×6) and calculations with and without spin-orbit coupling (SOC)

(i) Atomic structure



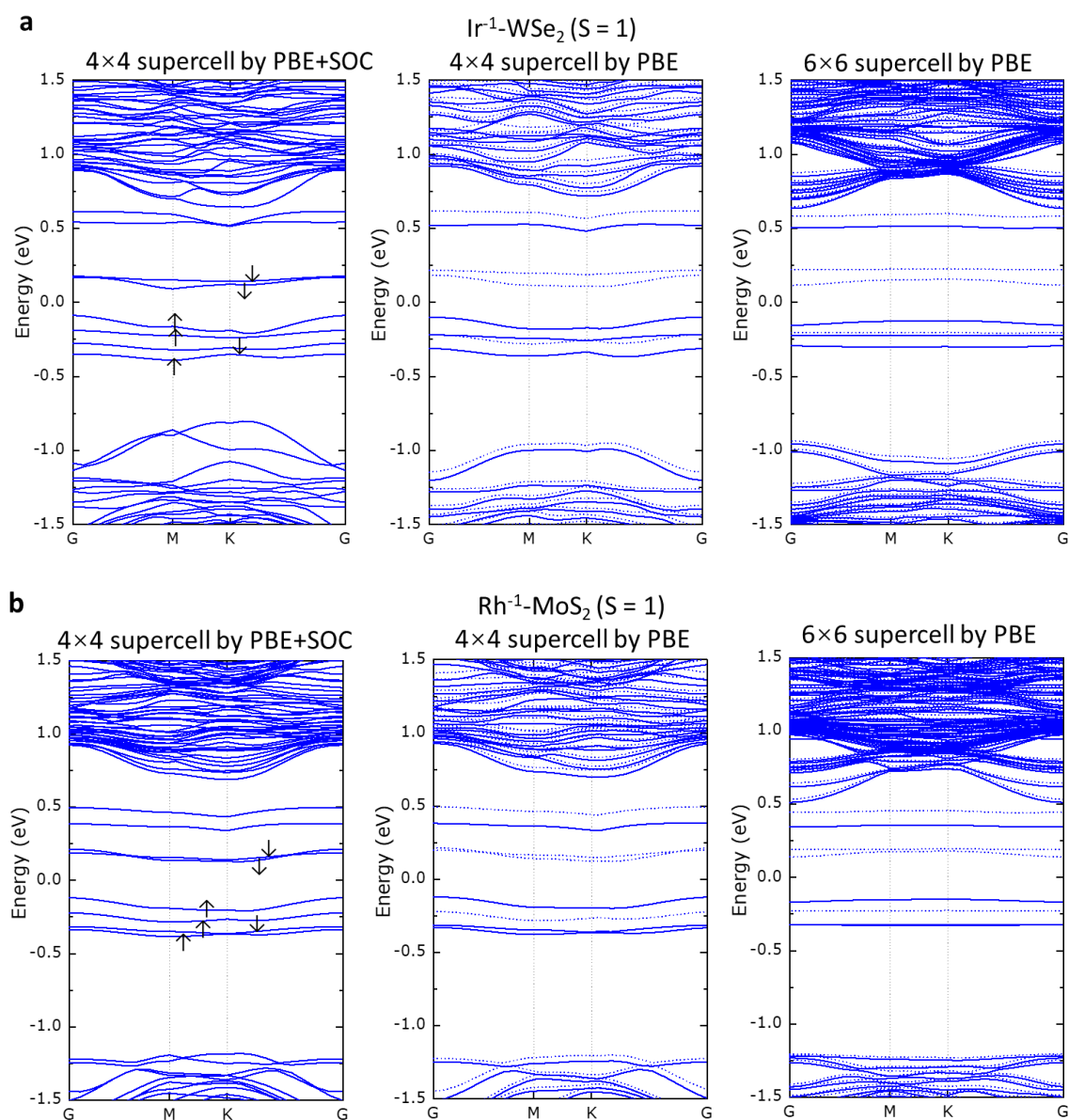
Supplementary Fig. 5 Relaxed structures of (a) Ir⁻¹-WSe₂ and (b) Rh⁻¹-MoS₂. Left: 4×4 supercell; Right 6×6 supercell.

(ii) Supplementary Table 8 Defect properties of Ir⁻¹-WSe₂ and Rh⁻¹-MoS₂ modelled using 4×4 and 6×6 supercells (PBE).

Supercell size	4×4	6×6
Defect properties	Ir⁻¹-WSe₂	
CTL (+1/0) (eV)	0.55	0.44
CTL (0/-1) (eV)	1.49	1.44
Singlet-Triplet gap (eV)	0.06	0.06
D^{SO} (THz)	8.69	7.91
ZPL _T (eV)	0.44	0.46
ZPL _{S1} (eV)	0.33	0.31
ZPL _{S2} (eV)	0.26	0.29
Defect properties	Rh⁻¹-MoS₂	
CTL (+1/0) (eV)	0.57	0.49
CTL (0/-1) (eV)	1.56	1.65
Singlet-Triplet gap (eV)	0.08	0.08
D^{SO} (THz)	0.98	0.87
ZPL _T (eV)	0.51	0.57
ZPL _S (eV)	0.27	0.30

Note that the D^{SO} calculated by PBE is significantly larger than obtained by HSE06. It has been found that the PBE functional tends to overestimate the SOC contribution to ZFS (nearly twofold discrepancy). This is intrinsically due to the underestimated energy gap between energy of different spin-state at PBE level, which in turn affects the ZFS calculation by SOC¹.

(iii) Band structures



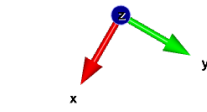
Supplementary Fig. 6 Band structures for (a) $\text{Ir}^{-1}\text{-WSe}_2$ and (b) $\text{Rh}^{-1}\text{-MoS}_2$. Left: 4×4 supercell with SOC; Middle: 4×4 supercell without SOC; Right: 6×6 supercell without SOC. The solid and dashed lines for band structures without SOC indicate the spin up and spin down states, respectively. The energies and spin states of the defect levels in the band gap are largely unchanged when compared to a 6×6 supercell or when compared to a band structure that includes the effects of SOC.

Supplementary Note 2: Defect energy level diagrams for selected symmetries

(i) Character tables of group D_{3h} , C_{2v} , and C_{1h}^2

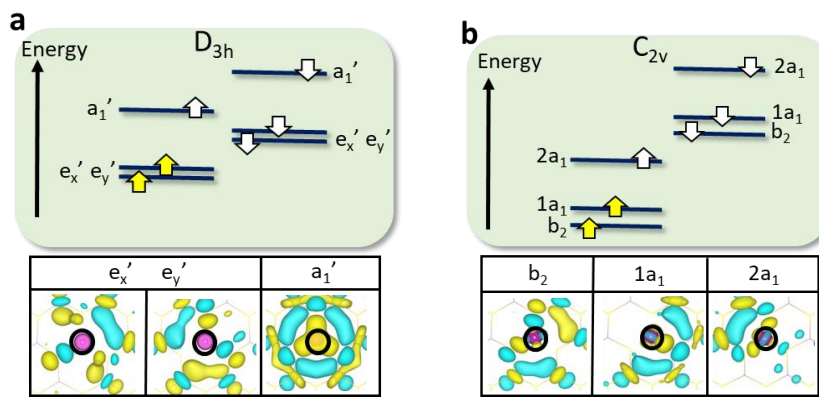
D_{3h}	E	$2C_3$	$3C_2'$	σ_h	$2S_3$	$3\sigma_v$	linear	quadratic
A_1'	+1	+1	+1	+1	+1	+1	x^2+y^2, z^2	
A_2'	+1	+1	-1	+1	+1	-1	R_z	
E'	+2	-1	0	2	-1	0	(x, y)	(x^2-y^2, xy)
A''_1	+1	+1	+1	-1	-1	-1		
A''_2	+1	+1	-1	-1	+1	+1	z	
E''	+2	-1	0	-2	+1	0	(R_x, R_y)	(xz, yz)

C_{2v}	E	C_2	$\sigma_v(yz)$	$\sigma_v(xy)$	linear	quadratic
A_1	+1	+1	+1	+1	y	x^2, y^2, z^2
A_2	+1	+1	-1	-1	R_y	xz
B_1	+1	-1	+1	-1	z, R_x	yz
B_2	+1	-1	-1	+1	x, R_z	xy



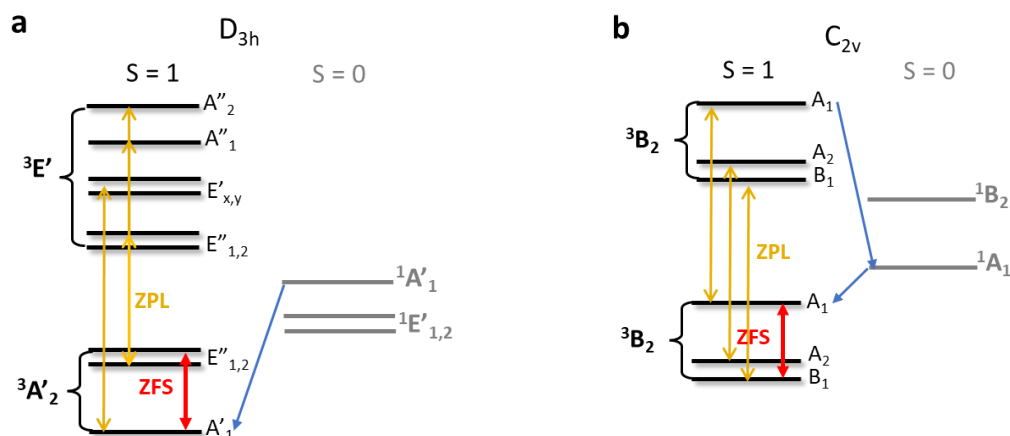
C_{1h}	E	σ_h	linear	quadratic
A'	+1	+1	x, y, R_z	x^2, y^2, z^2, xy
A''	+1	-1	z, R_x, R_y	xz, yz

(ii) Single-particle defect states



Supplementary Fig. 7 Schematic single-particle defect states and wavefunctions of (a) D_{3h} and (b) C_{2v} for $S = 1$. The yellow solid and hollow arrows mark the occupied and unoccupied in-gap defect states, respectively, which are labelled according to their IRs transforming under group symmetry. The corresponding real part of wavefunctions at the Gamma point are visualized in the top-view. The defect sites are circled in black.

(iii) Many-body level structure



Supplementary Fig. 8 Schematic many-body level structure of (a) D_{3h} and (b) C_{2v} with ZFS. The ZPL and ISC are marked.

Note that the discussion about C_{1h} can be found in Supplementary Fig. 2 for Rh⁻¹-MoS₂ and the main text Fig. 4 for Ir⁻¹-WSe₂.

Supplementary Note 3: Further details on the electronic structure for Ir⁻¹-WSe₂ and Rh⁻¹-MoS₂

(i) Supplementary Table 9 IRs of the spatial part of the many-body states, and ZPLs in Ir⁻¹-WSe₂ and Rh⁻¹-MoS₂.

Ir ⁻¹ -WSe ₂	T ₀	T ₁	S ₁ /S ₂	S ₀	ZPL (T ₀ -T ₁)	ZPL (S ₀ -S ₁)	ZPL (S ₀ -S ₂)
Hole representation	a''⊗a'	a''⊗a'	a'⊗a'	a''⊗a'	0.70 eV	0.62 eV	0.51 eV
Symbol	³ A''	³ A''	¹ A'	¹ A''	A' (x, y)	A'' (z)	A'' (z)

Rh ⁻¹ -MoS ₂	T ₀	T ₁	S ₁ /S ₂	S ₀	ZPL (T ₀ -T ₁)	ZPL (S ₀ -S ₁)	ZPL (S ₀ -S ₂)
Hole representation	a''⊗a'	a'⊗a'	a''⊗a''	a'⊗a''	0.94 eV	0.94 eV	0.81 eV
Symbol	³ A''	³ A'	¹ A'	¹ A''	A'' (z)	A'' (z)	A'' (z)

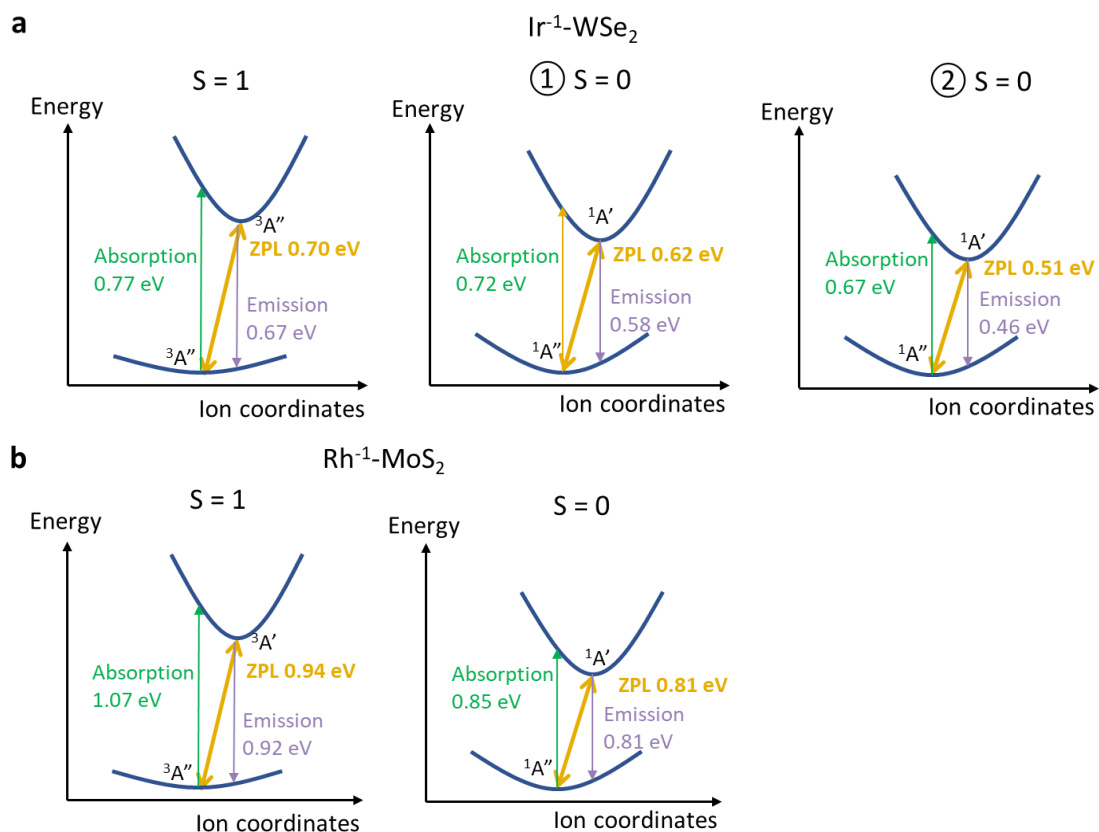
Note that the S₁ of Rh⁻¹-MoS₂ lies higher than the T₁, which is beyond the optical cycle of lower excited states. The ZPL transitions are optically allowed by linearly polarized light (see Fig. 4b of main text where the polarization direction is indicated) as derived from group theory.

(ii) Details on IRs for Ir⁻¹-WSe₂ (Fig. 4b)

The two-body wavefunctions transform as the direct product of spin double group IR, $D_{1/2} \otimes D_{1/2}$, which results in rotation functions of single group IRs under the integer total spin number. For C_{1h} symmetry in Ir⁻¹-WSe₂, the spin quantization axis is along the y direction as shown in Supplementary Note 1(i). The spin projections $\{S_y, S_z/S_x\}$ of spin-triplet configuration transform as $\{R_y, R_z/R_x\}$. Hence, $\{|0\rangle, |\pm\rangle\}$ correspond to $\{A'', A'/A''\}$. The spin-singlet configuration (zero-spin) corresponds to full symmetric IR $A'{}^2$.

The total many-body wavefunction is configured by a direct product of the IRs of the spatial and spin part under the point group symmetry³. The triplet ground state in the two-hole representation is $a''2a'$. It forms a spin-triplet manifold of $|{}^3A''\rangle$ with A' and A'' states of $|\pm\rangle$ and A' for a lower $|0\rangle$ state with spin projection $|S_x\rangle$, separated by 6.50 THz of $|D^{SO}|$. The rhombic ZFS for splitting between $|+\rangle$ and $|-\rangle$ is about 0.06 THz. The doublet $|\pm\rangle$ states are $|S_y\rangle$ and $|S_z\rangle$ spin projections. The spin-triplet excited state $a''1a'$ also has a spin-triplet manifold of $|{}^3A''\rangle$. Similarly, the spin-singlet excited and ground states can be expressed as $|{}^1A'_1\rangle$, $|{}^1A'_2\rangle$ and $|{}^1A''\rangle$. (Here, the subscript “1” and “2” are just symbols of distinct levels instead of other IRs).

(iii) Configuration coordinate diagram



Supplementary Fig. 9 Schematic configuration coordinate diagram of (a) Ir¹⁺-WSe₂ (include two pathways of spin singlet transition) and (b) Rh¹⁺-MoS₂ for transition between ground state and the lowest excited state for each spin multiplicity. The vertical absorption (green), ZPL (yellow), and vertical emission (pink) are marked.

References

1. Thiering, G. & Gali, A. Magneto-optical spectra of the split nickel-vacancy defect in diamond. *Phys Rev Res* **3**, 043052 (2021).
2. Dresselhaus, M. S., Dresselhaus, G. & Jorio, A. *Group theory: application to the physics of condensed matter*. (Springer Science & Business Media, 2007).
3. Maze, J. R. *et al.* Properties of nitrogen-vacancy centers in diamond: the group theoretic approach. *New J Phys* **13**, 025025 (2011).